INORGANIC CHEMISTRY FRONTIERS

RESEARCH ARTICLE

View Article Online
View Journal | View Issue

Cite this: *Inorg. Chem. Front.*, 2025, **12**, 8741

Charge compensation *via* tetravalent doping for high-efficiency Mn^{2+}-activated inorganic double perovskites toward high-resolution X-Ray imaging

Gaoyuan Xing,[a] Endian Cui,[a] Xiangyang Yuan,[a] Bing Wang,[b] Jiucun Chen,[a] Yanan Zhao,[c] Jianfeng Tang[a] and Jing Liu*[a]

In recent years, lead-free halide double perovskite nanocrystals (NCs) have emerged as compelling scintillator candidates due to their high effective atomic number, ultrafast scintillation decay kinetics, eco-friendly composition, and bandgap tunability, all of which are essential for high-temporal-resolution radiation detection. Although nanostructured scintillators achieve exceptional optical uniformity, their nanocrystalline forms exhibit inherent limitations in terms of light emission intensity and overall scintillation efficiency. A critical limitation of X-ray flat-panel minidetectors is the absence of novel engineering approaches to amplify radioluminescence capabilities. Herein, we engineered a charge compensation strategy for $Cs_2AgInCl_6$ double perovskite NCs through co-doping tetravalent ions with Mn^{2+} emissive centers to stabilize the heterovalent substitution of In^{3+} sites with Mn^{2+}. The co-doping of Zr^{4+} or Ce^{4+} enhanced Mn^{2+}-activated emission and induced sequential improvements in photoluminescence lifetime and quantum yield for CAIC:Mn^{2+}, CAIC:Mn^{2+},Zr^{4+} and CAIC:Mn^{2+},Ce^{4+}. XPS analysis confirmed 1.46-fold (CAIC:Mn^{2+},Zr^{4+}) and 1.59-fold (CAIC:Mn^{2+},Ce^{4+}) increases in the effective Mn^{2+}/Mn^{4+} doping concentration relative to CAIC:Mn^{2+}. Ce^{4+} effectively suppressed Mn^{2+} oxidation to higher valence states, enhancing the Mn^{2+}/Mn^{4+} ratio by 3.4 times. The CAIC:Mn^{2+},Ce^{4+}@PDMS scintillator film demonstrated a superior light yield of 16 807 photons MeV^{-1}, spatial resolution of 7.7 lp mm^{-1}, and detection limit of 619.2 nGy_{air} s^{-1}.

Received 25th July 2025,
Accepted 2nd October 2025

DOI: 10.1039/d5qi01582k

rsc.li/frontiers-inorganic

Introduction

Lead halide perovskite nanocrystals (NCs) have recently emerged as promising scintillator materials owing to their exceptional optoelectronic properties, including high photoluminescence quantum yields, superior X-ray absorption coefficients, rapid response characteristics, and tunable bandgaps *via* compositional engineering.[1,2] Liu *et al.* demonstrated $CsPbBr_3$ NCs with remarkable X-ray sensitivity, achieving a radioluminescence detection limit as low as 13 nGy_{air} s^{-1}, which is 423 times lower than the dose required for medical diagnosis.[3] However, the intrinsic toxicity of lead and environmental degradation of Pb-based perovskites under operational conditions impede their commercial viability, driving the exploration of lead-free alternatives.[4] Recent advances in lead substitution strategies focus on designing double perovskite with the general formula $A_2B_IB_{III}X_6$ (where A = monovalent cation, such as Cs^+; B_I = monovalent metal ions, such as Na^+ and Ag^+; B_{III} = trivalent metal ions, such as In^{3+} and Bi^{3+} and X = halogen anion, such as Cl^- and Br^-).[5,6] The dual-metal-site architecture further enables precise tuning of electronic and optical properties through compositional variation, offering a versatile platform to address the limitations of lead-based systems while retaining high-performance scintillation.[7–10] However, the absence of Pb in lead-free double perovskite still diminishes X-ray attenuation efficiency due to its lower effective atomic number than those of lead-containing counterparts, resulting in diminished radioluminescence intensity under equivalent irradiation doses. This inherent limitation significantly hinders their ability to achieve high-sensitivity, low-dose detection and sub-micron-scale spatial resolution. These performance indexes are crucial for meeting the requirements of next-generation medical diagnostics and non-destructive testing applications.[11–13]

The doping strategy of transition metal ions has emerged as an effective strategy for enhancing the scintillation perform-

[a]*Key Laboratory of Luminescence Analysis and Molecular Sensing, Ministry of Education, School of Materials and Energy, Southwest University, Chongqing, 400715, PR China. E-mail: jingliu77@swu.edu.cn*
[b]*Zolix Instruments Co., Ltd, Beijing 101102, China*
[c]*Analytical and Testing Center, Southwest University, Chongqing, 400715, PR China*

ance of lead-free halide double perovskite NCs.[9,14,15] As an economical and eco-friendly transition metal dopant, Mn^{2+} generates efficient luminescent centers *via* the $^4T_1 \rightarrow {}^6A_1$ transition in an octahedral coordinate, producing tunable broadband emission that spans the green-to-orange spectral range through crystal field modulation.[16,17] The extended carrier recombination lifetime of Mn^{2+} further enhances the photoluminescence quantum yield (PLQY) of the host matrix, enabling a high light yield under X-ray excitation.[16–19] Although Mn^{2+}-doped double perovskite NCs have been demonstrated as promising scintillation materials, their practical implementation remains hindered by the intrinsically low Mn^{2+} doping efficiency.[20–23] This limitation stems primarily from the non-equivalent substitution of the In^{3+} site by Mn^{2+} and lattice matching, which suppresses radiative recombination efficiency and ultimately degrades the luminescence performance of Mn^{2+}-doped double perovskite NCs.[24–26] This fundamental constraint underscores the imperative to develop innovative doping optimization strategies. Charge compensation has emerged as a promising approach to mitigate doping-induced defects, as evidenced by its successful implementation in conventional phosphors, where charge-balancing mechanisms effectively suppress substitution-related lattice distortions by maintaining valence equilibrium. Zhou *et al.* employed $Mg^{2+}/Zn^{2+}/Ca^{2+}$ co-doping in SrAl3BO7:Mn^{4+} to neutralize Mn^{4+}-induced charge imbalance, achieving 89% luminescence enhancement through defect suppression.[27] Zheng *et al.* developed a Be^{2+}-mediated charge compensation strategy in CaAl12O19:Mn^{4+} that simultaneously addresses charge imbalance and suppresses $Mn^{4+} \rightarrow Mn^{2+}$ self-reduction, achieving prominent luminescence enhancement with an internal quantum efficiency of 74.9% and external quantum efficiency of 56.3%.[28] Despite its proven efficacy in conventional phosphors, the charge compensation strategy remains conspicuously underexplored in double perovskite NCs, particularly for synchronously addressing doping limitations and enhancing scintillator performance.

In this study, we report significant enhancements in both the photoluminescence and radioluminescence of Mn^{2+}-doped $Cs_2AgInCl_6$ double perovskite NCs through co-doping with tetravalent ions (Ce^{4+} or Zr^{4+}). The underlying mechanism of the luminescence enhancement was investigated. The charge imbalance caused by the substitution of trivalent In^{3+} with divalent Mn^{2+} was rectified *via* Mn^{4+}–X^{4+} co-substitution for In^{3+}–In^{3+}. Notably, Ce^{4+} doping not only compensated for the charge imbalance but also suppressed the oxidation of Mn^{2+} to Mn^{4+}. This synergistically increased the effective doping amount of Mn and enhanced the Mn^{2+} relative occupancy of Mn^{2+}/Mn^{4+}. A flexible thin-film scintillator was fabricated by mixing PDMS with double perovskite NCs, resulting in an outstanding light yield of 16,807 photons per MeV, spatial resolution of 7.7 lp mm^{-1}, and detection limit of 619.2 nGy_{air} s^{-1}. Our study provides new insights into optimizing the scintillation performance of inorganic double perovskite NCs.

Results and discussion

$Cs_2AgInCl_6$:Mn^{2+} (CAIC:Mn^{2+}), $Cs_2AgInCl_6$:Mn^{2+},Zr^{4+} (CAIC:Mn^{2+},Zr^{4+}), and $Cs_2AgInCl_6$:Mn^{2+},Ce^{4+} (CAIC:Mn^{2+},Ce^{4+}) NCs were successfully synthesized through an optimized hot-injection protocol.[22] Fig. 1a illustrates the schematic crystallographic configurations of pristine CAIC, CAIC:Mn^{2+}, CAIC:Ce^{4+}, and CAIC:Mn^{2+},Ce^{4+}. As established in previous studies, under an octahedral coordination environment (CN = 6), the ionic radius of Mn^{2+} is 0.83 Å, and that of Ce^{4+} is 0.86 Å. These values closely match the ionic radius of In^{3+} (0.80 Å, CN = 6). This high degree of similarity in ionic size minimizes lattice strain and facilitates stable substitution at the In^{3+} site. This rationale is strongly supported by the results of previous theoretical and experimental studies.[22,29–32] The same site preference in analogous perovskite systems has been observed for other heterovalent cations with similar ionic radii, such as Te^{4+}.[33] All the X-ray diffraction (XRD) patterns of CAIC:Mn^{2+}, CAIC:Mn^{2+},Zr^{4+}, and CAIC:Mn^{2+},Ce^{4+} (Fig. 1b) clearly demonstrate characteristic diffraction peaks corresponding to the cubic phase structure of CAIC with space group $Fm\bar{3}m$ (ICSD No. 257115), indicating high crystallinity and the absence of impurity phases. Significantly, no obvious changes in the diffraction peaks were observed for the doped samples when compared with the undoped CAIC samples. This phenomenon can be reasonably explained by the low doping concentrations of Mn^{2+}, Zr^{4+}, and Ce^{4+} ions, which are less than 1% of the total ion content, consistent with previous reports.[21,29] The lattice parameters and unit cell dimensions of the prepared series of double perovskite NCs are summarized in Table S1. The lattice constants of CAIC:Mn^{2+}, CAIC:Mn^{2+},Zr^{4+}, and CAIC:Mn^{2+},Ce^{4+}

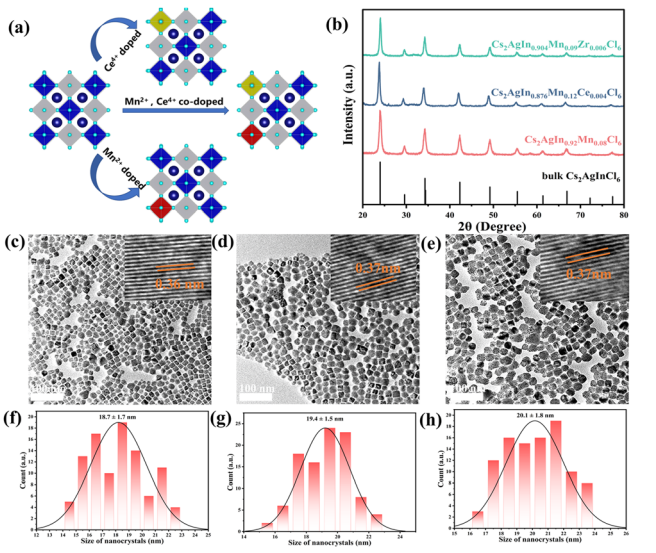

Fig. 1 (a) Schematic diagram of the crystal structure. (b) XRD patterns of CAIC:8%Mn^{2+}, CAIC:9%Mn^{2+},0.6%Zr^{4+} and CAIC:12%Mn^{2+},0.4%Ce^{4+} NCs. (c–e) TEM and HRTEM images of (c) CAIC:Mn^{2+}, (d) CAIC:Mn^{2+}, Zr^{4+} and (e) CAIC:Mn^{2+},Ce^{4+} NCs. (f–h) Size distribution estimated from TEM images of (f) CAIC:Mn^{2+}, (g) CAIC:Mn^{2+},Zr^{4+} and (h) CAIC:Mn^{2+}, Ce^{4+} NCs.

were determined to be 10.166 Å, 10.181 Å, and 10.192 Å, respectively. This progressive lattice dilatation correlates with the ionic radii hierarchy of the dopants (rCe^{4+} > rZr^{4+} > rMn^{2+}), confirming successful substitution at the octahedral sites.

The morphological and structural characteristics of the CAIC:Mn^{2+}, CAIC:Mn^{2+},Zr^{4+}, and CAIC:Mn^{2+},Ce^{4+} NCs were further investigated by transmission electron microscopy (TEM) and high-resolution TEM (HRTEM). The low-magnification TEM images (Fig. 1c–e) reveal uniformly dispersed double perovskite NCs with cubic morphology. The average sizes of CAIC:Mn^{2+}, CAIC:Mn^{2+},Zr^{4+}, and CAIC:Mn^{2+},Ce^{4+} NCs are approximately 18.7 nm, 19.4 nm, and 20.1 nm, respectively, indicating a systematic size increase that correlates with dopant ionic radii (Fig. 1f–h). The HRTEM images (insets in Fig. 1c–e) demonstrate that all the samples possess similar phase structures, confirming their high crystallinity. The measured interplanar spacing of the (220) crystal plane increases sequentially from 0.36 nm (CAIC:Mn^{2+}) to 0.37 nm (CAIC:Mn^{2+},Zr^{4+} and CAIC:Mn^{2+},Ce^{4+}). This observation is consistent with the lattice parameter variations deduced from the XRD analysis. Ion doping has no significant influence on the morphology and crystallinity of the double perovskite NCs.

X-ray photoelectron spectroscopy (XPS) was systematically employed to probe the elemental doping states and compositional evolution in the CAIC:Mn^{2+}, CAIC:Mn^{2+},Zr^{4+}, and CAIC:Mn^{2+},Ce^{4+} NCs. As illustrated in Fig. 2, the XPS spectra of all three samples confirm the presence of Cs, Ag, In, Cl, and Mn elements. Specifically, the high-resolution XPS spectra of Zr 4d and Ce 3d for the CAIC:Mn^{2+},Zr^{4+} and CAIC:Mn^{2+},Ce^{4+} NCs (Fig. S1) validate the successful incorporation of Zr and Ce dopants, respectively. Additionally, the quantitative analysis of the elemental contents, which was derived from the XPS results, is summarized in Table S2. The XPS results revealed a 46% and 60% enhancement in Mn incorporation efficiency for Zr^{4+}- and Ce^{4+}-co-doped systems, respectively, compared to singly Mn^{2+}-doped CAIC. This synergistic doping effect possibly originates from charge compensation mechanisms, wherein higher-valent Zr^{4+} and Ce^{4+} substitutions at In^{3+} sites stabilize Mn^{2+} occupancy through electrostatic balancing.[34]

Photoluminescence spectroscopy was utilized to systematically investigate the effects of charge compensation on the optical properties of Mn^{2+}-doped double perovskite NCs. CAIC:Mn^{2+} exhibits a distinct photoluminescence emission peak centered at 620 nm under 310 nm excitation, corresponding to the spin-forbidden $^4T_1(g) \rightarrow {}^6A_1(S)$ d–d transition of Mn^{2+} ions in octahedral coordination (Fig. S2a).[21–23] The excitation spectrum of CAIC:Mn^{2+} exhibits a bimodal profile in the ultraviolet regime, with principal excitation maxima at 254 and 320 nm, corresponding to spin–orbit coupling-induced $^1S_0 \rightarrow {}^3P_2$ and $^1S_0 \rightarrow {}^3P_1$ transitions of Mn^{2+}, respectively.[23] The concentration-dependent luminescent behavior of CAIC:Mn^{2+} was investigated. The photoluminescence emission intensity of CAIC:Mn^{2+} exhibits an initial increase as the doping concentration of Mn^{2+} increases from 10% to 20% and then decreases when further increasing to 30% (Fig. S2b), which is possibly due to the concentration quenching effect mediated by Mn–Cl–Mn exchange interaction and the proliferation of non-radiative recombination centers.[21] A systematic comparison of photophysical properties, including emission spectral profiles, excited-state lifetimes and PLQY, was conducted among CAIC:Mn^{2+}, CAIC:Mn^{2+},Zr^{4+} and CAIC:Mn^{2+},Ce^{4+}. Fig. 3a and b show the concentration-dependent emission spectra of CAIC:Mn^{2+}, Zr^{4+} and CAIC:Mn^{2+},Ce^{4+}, where (a) corresponds to the Zr^{4+} concentration series (0–5 mol%) and (b) depicts the Ce^{4+} concentration gradient (0–5 mol%), maintaining a constant Mn^{2+} doping level at 20 mol%. It is observed that as the doping levels of Zr^{4+} and Ce^{4+} increase, the emission intensity of Mn^{2+} first increases and then decreases, yet remains higher than that of single-doped CAIC:Mn^{2+}, proving that the incorporation of Zr^{4+} and Ce^{4+} evidently enhances Mn^{2+} emission intensity. The intensities reached a maximum at the critical concentrations of 3 mol% Zr^{4+} and 2 mol% Ce^{4+}. This intensity decrease may result from the accelerated formation of non-radiative recombination centers and defects.[23,29,35,36] CAIC:Mn^{2+},Ce^{4+} exhibits a more pronounced optimization effect than CAIC:Mn^{2+},Zr^{4+} (Fig. 3c). The excitation spectra of CAIC:Mn^{2+},Zr^{4+} and CAIC:Mn^{2+},Ce^{4+} show a subtle blue-shift relative to CAIC:Mn^{2+} (Fig. S3), which may result from the expanded double-perovskite band gap upon the incorporation of Zr^{4+} or Ce^{4+}.[35,36]

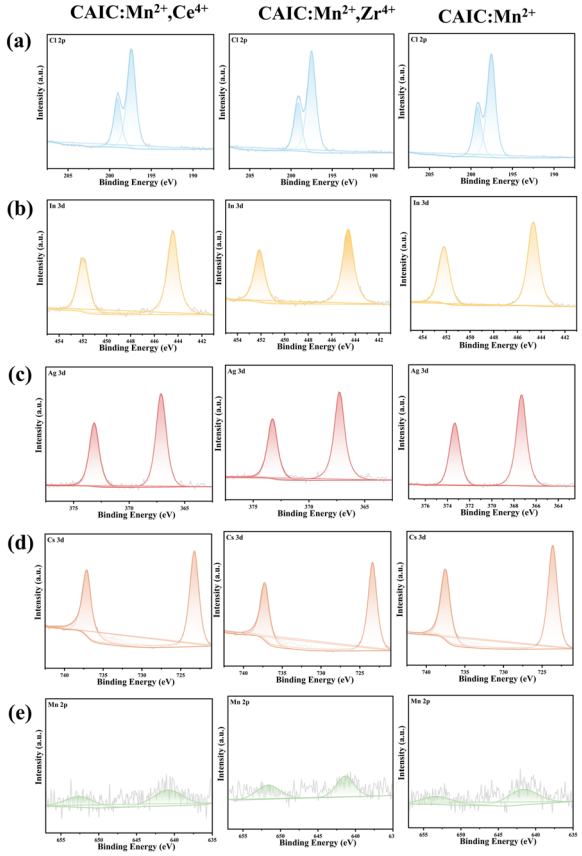

Fig. 2 (a–e) High-resolution XPS spectra of (a) Cl 2p, (b) In 3d, (c) Ag 3d, (d) Cs 3d, and (e) Mn 2p for CAIC:Mn^{2+}, CAIC:Mn^{2+},Zr^{4+} and CAIC:Mn^{2+},Ce^{4+} NCs.

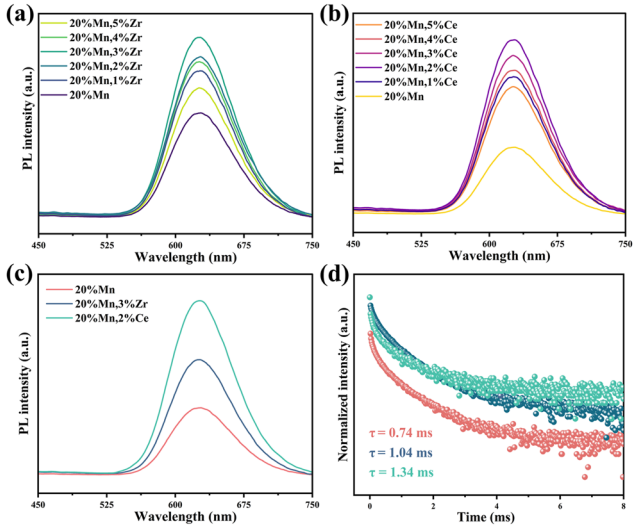

Fig. 3 (a) Photoluminescence spectra (λ_{ex} = 310 nm) of CAIC:20% Mn^{2+},*x*% Zr^{4+} (*x* = 0, 1, 2, 3, 4, 5) NCs. (b) Photoluminescence spectra (λ_{ex} = 310 nm) of CAIC:20% Mn^{2+},*y*% Ce^{4+} (*y* = 0, 1, 2, 3, 4, 5) NCs. (c) Photoluminescence spectra (λ_{ex} = 310 nm) of CAIC:Mn^{2+}, CAIC:Mn^{2+}, Zr^{4+} and CAIC:Mn^{2+},Ce^{4+}. (d) Photoluminescence lifetime decay curves of CAIC:Mn^{2+}, CAIC:Mn^{2+},Zr^{4+} and CAIC:Mn^{2+},Ce^{4+} (λ_{ex} = 310 nm, λ_{ex} = 620 nm).

The photoluminescence lifetime decay curves of CAIC:Mn^{2+}, CAIC:Mn^{2+},Zr^{4+} and CAIC:Mn^{2+},Ce^{4+} are shown in Fig. 3d. The average lifetime τ_{ave} can be calculated using the following formula:[21,23,29]

$$\tau_{ave} = \frac{A_1 \cdot \tau_1^2 + A_2 \cdot \tau_2^2}{A_1 \cdot \tau_1 + A_2 \cdot \tau_2},$$

where A_1 and A_2 represent the amplitudes of the two signal components, and τ_1 and τ_2 are the corresponding time constants, respectively. The measured lifetimes of CAIC:Mn^{2+}, CAIC:Mn^{2+},Zr^{4+}, and CAIC:Mn^{2+},Ce^{4+} are 0.74, 1.04, and 1.34 ms, respectively (Table S4), which fall within the millisecond range and are comparable to those reported for other Mn^{2+}-doped scintillations.[37–39] The PLQYs of CAIC:Mn^{2+}, CAIC:Mn^{2+},Zr^{4+} and CAIC:Mn^{2+},Ce^{4+} are 6.72%, 13.22% and 18.46%, respectively (Fig. S4). The significant increase in both the lifetime and PLQY indicates that the incorporation of Zr^{4+} and Ce^{4+} reduces the non-radiative transitions of Mn^{2+} and improves the luminescence properties of CAIC:Mn^{2+}.

The aliovalent substitution mechanisms in Mn^{2+}-mono-doped, and Mn^{2+}, X^{4+} (X = Zr, Ce) co-doped CAIC double perovskite NCs were analyzed. When Mn^{2+} substitutes for In^{3+} sites, charge non-equivalence is introduced due to the valence difference (+3 for In^{3+} *vs.* +2 for Mn^{2+}), generating In cation vacancies. To maintain the charge balance in the CAIC host lattice, the substitution of trivalent In^{3+} by divalent Mn^{2+} follows a stoichiometric charge compensation ratio of 3 : 2. During the doping process, each Mn^{2+} replacing an In^{3+} generates a negatively charged defect ($[Mn^{2+}]_{In}^{'}$) and a positively charged vacancy ($V_{In}^{\bullet}$), as described by process (1). The positively charged vacancy $V_{In}^{\bullet}$ is energetically unstable and tends to capture electrons to reach equilibrium, potentially oxidizing Mn^{2+} to a higher valence state (*e.g.*, Mn^{4+}), as shown in processes (2) and (3).[40–42]

$$Mn^{2+} + In^{3+} \rightarrow [Mn^{2+}]_{In}^{'} + V_{In}^{\bullet} \quad (1)$$

$$V_{In}^{\bullet} + e^{-} \rightarrow V_{In}^{\times} \quad (2)$$

$$[Mn^{2+}]_{In}^{'} \rightarrow [Mn^{4+}]_{In}^{\bullet} + 2e^{-} \quad (3)$$

When tetravalent ions X^{4+} (X = Zr, Ce) are incorporated into CAIC:Mn^{2+}, each X^{4+} substitution for In^{3+} generates a positively charged defect ($[X^{4+}]_{In}^{\bullet}$) and a negatively charged vacancy ($V_{In}^{'}$), as described by process (4). The negatively charged vacancy $V_{In}^{'}$ tends to release electrons to achieve charge equilibrium, counteracting the electron capture process (2). Specifically, the negatively charged $V_{In}^{'}$ and positively charged $V_{In}^{\bullet}$ can neutralize each other to reach equilibrium, as shown in process (5).[41,42] Additionally, the positively charged $[X^{4+}]_{In}^{\bullet}$ and negatively charged $[Mn^{2+}]_{In}^{'}$ defects can balance charges through process (6). This interaction effectively hinders the progression of process (3), thereby suppressing the oxidation of Mn^{2+} to a higher valence state.[34,41,42]

$$X^{4+} + In^{3+} \rightarrow [X^{4+}]_{In}^{\bullet} + V_{In}^{'} \quad (4)$$

$$V_{In}^{'} + V_{In}^{\bullet} \rightarrow V_{In}^{\times} \quad (5)$$

$$[X^{4+}]_{In}^{\bullet} + [Mn^{2+}]_{In}^{'} \rightarrow [X^{4+}]_{In}^{\times} + [Mn^{2+}]_{In}^{\times} \quad (6)$$

More intriguingly, compared to Zr^{4+}, Ce^{4+} facilitates charge compensation and introduces a dynamic redox equilibrium through the Ce^{4+}/Ce^{3+} ion pair, which further suppresses the oxidation of Mn^{2+} to higher valence states. Consequently, Ce^{4+} exhibits superior optimization of Mn^{2+} emission.[41] The Ce 3d XPS spectra can be deconvoluted into two spin–orbit components, $3d_{5/2}$ and $3d_{3/2}$, corresponding to the Ce^{3+} and Ce^{4+} oxidation states of Ce, respectively.[43,44] As evidenced by XPS analysis in Fig. S5a, both Ce^{3+} and Ce^{4+} coexist in CAIC:Ce^{4+} and CAIC:Mn^{2+},Ce^{4+}. Notably, the Ce^{4+}/Ce^{3+} ratio increases significantly from 0.69 (CAIC:Ce^{4+}) to 1.27 in the CAIC:Mn^{2+},Ce^{4+} (Fig. S5b). This observation stems from the substitution of trivalent In^{3+} by tetravalent Ce^{4+}, which generates positively charged defects $[Ce^{4+}]_{In}^{\bullet}$. These defects exhibit a high affinity for electron capture, driving their reduction to Ce^{3+} and establishing a Ce^{4+}/Ce^{3+} redox equilibrium within the lattice.[30,41,42,45] Consequently, to maintain charge neutrality, a higher proportion of Ce^{3+} compared to Ce^{4+} was observed in the CAIC:Ce^{4+} sample. For CAIC:Mn^{2+},Ce^{4+}, the charge compensation mechanism between Ce^{4+} and Mn^{2+} (process (6)), and redox interactions between the Ce^{4+}–Ce^{3+} and Mn^{2+}–Mn^{4+} lead to a decrease in the trivalent Ce^{3+} proportion and an increase in the tetravalent Ce^{4+}. To further illustrate the impact of charge compensation on the Mn^{2+}–Mn^{4+} conversion, the high-resolution Mn 2p XPS spectra were obtained for CAIC:Mn^{2+}, CAIC:Mn^{2+},Zr^{4+} and CAIC:Mn^{2+},Ce^{4+} (Fig. S6a). The Mn $2p_{3/2}$ XPS spectra can be deconvoluted into distinct peaks at

640 eV (Mn^{2+}) and 642 eV (Mn^{4+}).[28] Remarkably, the effective doping content of Mn^{2+} at 640 eV is significantly higher than that of Mn^{4+} at 642 eV after co-doping with Zr^{4+} or Ce^{4+}. To more intuitively visualize the changes in the proportions of Mn ions in different valence states, further integration of XPS fitting results was performed. The proportions of Mn^{2+} in both CAIC:Mn^{2+},Zr^{4+} and CAIC:Mn^{2+},Ce^{4+} increase significantly, with CAIC:Mn^{2+},Ce^{4+} exhibiting a more pronounced optimization effect (Fig. S6b). The Mn^{2+}/Mn^{4+} ratio of CAIC:Mn^{2+},Ce^{4+} (4.58) is 3.4-fold higher than that of CAIC:Mn^{2+} (1.33) and 1.4-fold higher than that of CAIC:Mn^{2+},Zr^{4+} (3.22), while CAIC:Mn^{2+},Zr^{4+} exhibits a 2.4-fold increase in the Mn^{2+}/Mn^{4+} ratio compared to CAIC:Mn^{2+}. These results confirm that the charge compensation effect stabilizes Mn^{2+} within the lattice, optimizing its luminescent properties. Furthermore, upon self-reduction of Ce^{4+} to Ce^{3+}, energy transfer to Mn^{2+} occurs, further intensifying its emission.[46]

XPS quantitative analysis further demonstrated that Zr^{4+} or Ce^{4+} co-doping significantly enhances Mn^{2+}/Mn^{4+} incorporation efficiency, with effective doping concentration increasing to 1.46 times (Zr^{4+}) and 1.59 times (Ce^{4+}) relative to the CAIC:Mn^{2+} sample, as quantified by peak-area integration of Mn $2p_{3/2}$ orbitals (Table S2). ICP-OES elemental analysis was also performed to monitor cationic stoichiometric evolution before and after tetravalent doping. Zr^{4+} or Ce^{4+} co-doping increased the effective Mn^{2+}/Mn^{4+} doping amounts by 1.12-fold and 1.5-fold, respectively, with the most pronounced augmentation observed in CAIC:Mn^{2+},Ce^{4+} (Table S3). This aligns with XPS elemental analysis, further validating that the charge compensation effect enhances the effective incorporation of Mn^{2+}/Mn^{4+} into the lattice. The co-doping of tetravalent cations (Zr^{4+}, Ce^{4+}) into CAIC:Mn^{2+} substantially reduces the defect density induced by the non-isovalent Mn^{2+} substitution at the In^{3+} sites in double perovskite NCs, simultaneously increasing the effective Mn^{2+}/Mn^{4+} doping concentration and optimizing its luminescent performance.

Previous studies have confirmed that charge compensation engineering effectively enhances the photoluminescence efficiency of CAIC:Mn^{2+}; however, its influence on radiation-induced luminescence remains unexplored. Given the critical dependence of scintillator performance on defect density, carrier mobility, and exciton self-trapping dynamics, the scintillation characteristics of CAIC:Mn^{2+}, CAIC:Mn^{2+},Zr^{4+} and CAIC:Mn^{2+},Ce^{4+} have been systematically investigated. First, we evaluated the X-ray absorption coefficients of CAIC:Mn^{2+},Ce^{4+} against commercial scintillators ($CsPbBr_3$, Si, CsI:Tl, and YAG:Ce) based on the photon cross-section database. As illustrated in Fig. 4a, CAIC:Mn^{2+},Zr^{4+} presents superior absorption efficiency across the photon energy range from 1 keV to 100 MeV, significantly outperforming YAG:Ce and Si. Additionally, its X-ray absorption rates are comparable to commercial scintillators $CsPbBr_3$ and CsI:Tl. The X-ray absorption efficiency of a material exhibits a linear dependence on its thickness. The thickness-dependent X-ray attenuation efficiency of CAIC:Mn^{2+},Ce^{4+}, CsI:Tl, and YAG:Ce was quantified at a fixed X-ray photon energy of 22 keV (Fig. 4b). The synthesized CAIC:Mn^{2+}, Ce^{4+} demonstrates excellent X-ray attenuation efficiency compared to CsI:Tl and YAG:Ce within the thickness range of 0–1.5 mm. CAIC:Mn^{2+},Ce^{4+} scintillator achieves complete absorption of X-ray energy at 0.75 mm, highlighting its potential as a high-performance X-ray-absorbing scintillation material for practical applications.

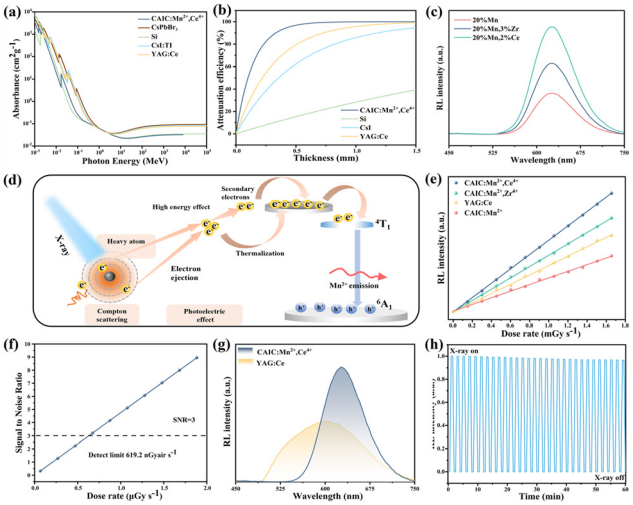

Fig. 4 (a) X-ray absorption coefficients of $CsPbBr_3$, Si, CsI-Tl, YAG:Ce and CAIC:Mn^{2+},Ce^{4+} scintillators as a function of photon energy. (b) Attenuation efficiency of Si, CsI-Tl, YAG:Ce and CAIC:Mn^{2+},Ce^{4+} scintillators as a function of thickness under 22 keV X-ray photon radiation. (c) Radioluminescence spectra of CAIC:Mn^{2+}, CAIC:Mn^{2+},Zr^{4+} and CAIC:Mn^{2+},Ce^{4+}. (d) Proposed radioluminescence mechanism diagram. (e) Radioluminescence intensities of CAIC:Mn^{2+}, CAIC:Mn^{2+},Zr^{4+}, CAIC:Mn^{2+},Ce^{4+} and YAG:Ce scintillators as a function of X-ray dose rate. (f) SNR values of CAIC:Mn^{2+},Ce^{4+} as a function of an X-ray dose rate. (g) Radioluminescence spectra of CAIC:Mn^{2+},Ce^{4+} and YAG:Ce scintillators. (h) Radioluminescence intensity of CAIC:Mn^{2+},Ce^{4+} over 30 consecutive X-ray irradiation on/off cycles (beam current: 100 μA, tube voltage: 50 kV).

The radioluminescence spectra of CAIC:Mn^{2+}, CAIC:Mn^{2+},Zr^{4+} and CAIC:Mn^{2+},Ce^{4+} are shown in Fig. 4c. A sequential radioluminescence intensity enhancement is observed: CAIC:Mn^{2+} < CAIC:Mn^{2+},Zr^{4+} < CAIC:Mn^{2+},Ce^{4+}, aligning with the corresponding photoluminescence trends shown in Fig. 3c. Specifically, in the absence of charge compensation, lattice charge neutrality is maintained by generating cation vacancies (such as In vacancy $V_{In}^{\bullet\bullet\bullet}$).[47–49] These vacancies act as non-radiative recombination centers, leading to the quenching of active luminescent centers. In contrast, the co-doping of Ce^{4+} and Zr^{4+} as charge compensators effectively eliminates the non-radiative recombination centers, thereby enhancing the emission intensity.[29] The proposed radioluminescence mechanism (Fig. 4d) highlights a critical distinction from the photoluminescence process. Radioluminescence involves an additional energy relaxation and thermalization process of high-energy electrons generated *via* X-ray interactions. X-ray photons first interact with the heavy atoms in the CAIC:Mn^{2+}, Ce^{4+} scintillator. Through the photoelectric effect and Compton scattering, the atoms absorb radiation energy *via*

electron excitation: the photoelectric effect ejects electrons directly, while Compton scattering generates high-energy electrons. These high-energy electrons undergo thermalization on an ultrafast timescale, which simultaneously loses energy through inelastic collisions with lattice constituents, thereby inducing secondary electron generation. The primary ejected electrons and secondary electrons generated by irradiation eventually become trapped by Mn^{2+} luminescent centers. Subsequently, these centers release energy *via* radiative transitions, producing intense red radioluminescence.[31,50–53] A detailed energy level diagram illustrating this process for Mn^{2+} is shown in Fig. S8.

The X-ray dose rate dependence of the radioluminescence intensities of CAIC:Mn^{2+}, CAIC:Mn^{2+},Zr^{4+} and CAIC:Mn^{2+},Ce^{4+} scintillators was recorded (Fig. 4e). These scintillators consistently exhibit a broad linear response within the dose rate range of 0.15–1.65 mGy_{air} s^{-1}. The radioluminescence intensity of CAIC: Mn^{2+},Ce^{4+} is higher than that of YAG:Ce at an equivalent X-ray dose rate, highlighting its superior X-ray detection sensitivity. The detection limit, defined as the dose rate corresponding to a signal-to-noise ratio (SNR) of 3, was calculated as 619.2 nGy_{air} s^{-1} for CAIC:Mn^{2+},Ce^{4+} (Fig. 4f). This value achieves a 8.6-fold reduction compared to the medical diagnostic standard of 5.5 μGy_{air} s^{-1}. The light yield, a crucial parameter for determining scintillator performance and high-resolution X-ray imaging capability, quantifies photon emission per unit of absorbed ionizing energy. The light yield of CAIC:Mn^{2+},Ce^{4+} scintillator was determined to be 16 807 photons per MeV using a commercial YAG:Ce single crystal (14 000 photons per MeV) as a calibration standard under identical X-ray tube operating conditions (Fig. 4g). The radioluminescence intensity of the CAIC:Mn^{2+},Ce^{4+} scintillator remained nearly unchanged over 30 consecutive on/off cycles when exposed to an X-ray source with a tube current of 100 μA and a tube voltage of 50 kV (Fig. 4h). The scintillator's excellent stability under X-ray irradiation demonstrates its practical application potential. Furthermore, no discernible changes were observed in the XRD diffraction pattern of CAIC:Mn^{2+},Ce^{4+} after prolonged X-ray exposure (Fig. S7), indicating its outstanding structural stability and resistance to radiation-induced degradation.

Finally, we evaluated the X-ray imaging performance of the scintillators using a custom-designed system (Fig. 5a). The CAIC:Mn^{2+},Ce^{4+}@PDMS scintillator film exhibits bright red photoluminescence under ultraviolet irradiation. Critically, it demonstrates exceptional spatial uniformity across the entire film, in addition to excellent flexibility that allows for easy folding and twisting (Fig. 5b and c). The profile of a metal key was well resolved under X-ray irradiation (Fig. S6d and e). The metal spring enclosed within the ball-point pen was invisible to the naked eye under daylight conditions; however, the internal structural outline of the spring enclosed within the pen was distinctly revealed under X-ray illumination (Fig. 5f and g). To quantify spatial resolution, the modulation transfer function (MTF) was derived *via* a slanted-edge analysis of the acquired radiographs. The spatial resolution is 7.7 lp mm^{-1} at

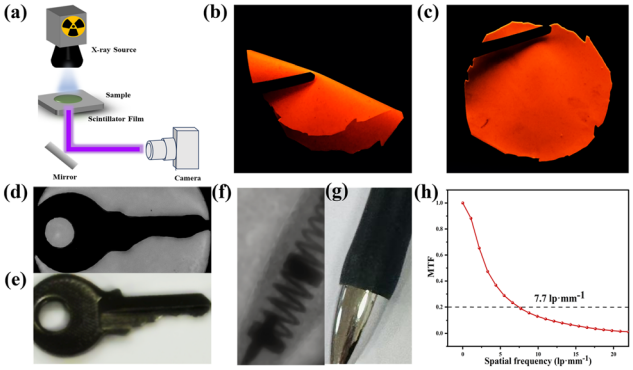

Fig. 5 (a) Schematic diagram of a custom-designed X-ray imaging system. (b and c) Photographs of the CAIC:Mn^{2+},Ce^{4+}@PDMS film under an ultraviolet lamp (290 nm). (d and e) Images of a metal key under the illumination of (d) X-ray and (e) daylight. (f and g) Images of a ballpoint pen under the illumination of (f) X-ray and (g) daylight. (h) MTF curve of the CAIC:Mn^{2+},Ce^{4+}@PDMS film measured using the slanted-edge method.

an MTF value of 0.2 (Fig. 5h). This result indicates that X-ray images generated by CAIC:Mn^{2+},Ce^{4+}@PDMS scintillator screen exhibit high resolution, validating their practical viability for non-destructive evaluation of complex components and highlighting their exceptional performance in high-resolution X-ray imaging.

Conclusion

In conclusion, a series of Mn^{2+}-doped CAIC double perovskite NCs were synthesized using an optimized hot-injection method. A rational charge compensation strategy *via* co-doping with tetravalent cations (Zr^{4+} or Ce^{4+}) was implemented to enhance their photoluminescence properties. The introduction of Zr^{4+} and Ce^{4+} significantly amplified Mn^{2+}-activated emission intensity, with lifetimes increasing sequentially from 0.74 ms (CAIC:Mn^{2+}) to 1.04 ms (CAIC:Mn^{2+},Zr^{4+}) and 1.34 ms (CAIC:Mn^{2+},Ce^{4+}). The corresponding PLQY improved from 6.72% (CAIC:Mn^{2+}) to 13.22% (CAIC:Mn^{2+},Zr^{4+}) and 18.46% (CAIC:Mn^{2+},Ce^{4+}). XPS quantitative analysis confirmed a 1.46-fold (CAIC:Mn^{2+},Zr^{4+}) and 1.59-fold (CAIC:Mn^{2+},Ce^{4+}) increase in the effective doping concentration of Mn^{2+}/Mn^{4+} relative to CAIC:Mn^{2+}. The redox-active Ce^{4+} effectively suppressed Mn^{2+} oxidation to higher valence states, yielding a 3.4-fold enhancement in Mn^{2+}/Mn^{4+} ratio for CAIC:Mn^{2+},Ce^{4+} compared to CAIC:Mn^{2+}, while CAIC:Mn^{2+},Zr^{4+} achieved a 2.4-fold improvement. The influence of the charge compensation effect on radiation-induced luminescence was also explored. The CAIC:Mn^{2+},Ce^{4+}@PDMS scintillator film exhibited intense red radioluminescence under X-ray irradiation, featuring a higher light yield than the commercial scintillator YAG:Ce single crystal. The scintillator film demonstrated a spatial resolution of 7.7 lp mm^{-1} and a low detection limit of 619.2 nGy_{air} s^{-1}. Furthermore, its excellent radiation stability and prolonged operational lifetime under continuous X-ray irradiation signifi-

cantly facilitate the practical application of inorganic nanoscintillators in high-resolution X-ray microimaging.

Author contributions

Gaoyuan Xing: writing – original draft, investigation, data curation. Endian Cui and Xiangyang Yuan: data curation, visualization. Bing Wang: resources. Yanan Zhao, Jianfeng Tang: supervision, conceptualization, resources. Jiucun Chen: resources. Jing Liu: supervision, writing – review & editing.

Data availability

The data supporting this article have been included as part of the supplementary information (SI). Supplementary information contains a detailed Experimental Section, and characterization data: photoluminescence excitation spectra, photoluminescence emission spectra, PLQYs, XPS analyses, XRD spectra, *etc*. See DOI: **https://doi.org/10.1039/d5qi01582k**.

Conflicts of interest

There are no conflicts to declare.

Acknowledgements

This research was supported by the Science and Technology Research Program of Chongqing Municipal Education Commission (Grant No. KJZD-K202400201, and KJQN202200221), Fundamental Research Funds for the Central Universities (SWU-KT25003), and the Natural Science Foundation of Chongqing (CSTB2024NSCQ-MSX0459). We acknowledge the critical and quantity of testing work supported by Beijing Zhongkebaice Technology Service Co., Ltd. We thank Prof. Yingshuai Liu for his guidance. We thank Analytical and Testing Center of Southwest University for their assistance with UV-Vis absorption spectra and photoluminescence spectra measurements. We thank Zolix Instruments Co., Ltd for assisting with X-ray imaging.

References

1 Y. Wang, M. Li, Z. Chai, Y. Wang and S. Wang, Perovskite scintillators for improved X-ray detection and imaging, *Angew. Chem., Int. Ed.*, 2023, **62**, e202304638.
2 Z. Xiao, Z. Song and Y. Yan, From lead halide perovskites to lead-free metal halide perovskites and perovskite derivatives, *Adv. Mater.*, 2019, **31**, 1803792.
3 Q. Chen, J. Wu, X. Ou, B. Huang, J. Almutlaq, A. A. Zhumekenov, X. Guan, S. Han, L. Liang, Z. Yi, J. Li, X. Xie, Y. Wang, Y. Li, D. Fan, D. B. L. Teh, A. H. All, O. F. Mohammed, O. M. Bakr, T. Wu, M. Bettinelli, H. Yang, W. Huang and X. Liu, All-inorganic perovskite nanocrystal scintillators, *Nature*, 2018, **561**, 88–93.
4 Y. Liu, A. Nag, L. Manna and Z. Xia, Lead-free double perovskite $Cs_2AgInCl_6$, *Angew. Chem., Int. Ed.*, 2021, **60**, 11592–11603.
5 H. Lei, D. Hardy and F. Gao, Lead-free double perovskite $Cs_2AgBiBr_6$: fundamentals, applications, and perspectives, *Adv. Funct. Mater.*, 2021, **31**, 2105898.
6 B. Yang, J. Chen, S. Yang, F. Hong, L. Sun, P. Han, T. Pullerits, W. Deng and K. Han, Lead-free silver-bismuth halide double perovskite nanocrystals, *Angew. Chem., Int. Ed.*, 2018, **57**, 5359–5363.
7 N. Ali, K. Shehzad, S. Attique, A. Ali, F. Akram, A. Younis, S. Ali, Y. Sun, G. Yu, H. Wu and N. Dai, Exploring non-toxic lower dimensional perovskites for next-generation X-ray detectors, *Small*, 2024, **20**, 2310946.
8 X. Wu, A. Li, M. Yang, X. Hao, L. Wu, R. Su and J. Zhang, Development of high-performance direct X-ray detector materials: from hybrid halide perovskites to all-inorganic lead-free perovskites, *J. Mater. Chem. C*, 2024, **12**, 8647–8667.
9 W. Zhu, W. Ma, Y. Su, Z. Chen, X. Chen, Y. Ma, L. Bai, W. Xiao, T. Liu, H. Zhu, X. Liu, H. Liu, X. Liu and Y. Yang, Low-dose real-time X-ray imaging with nontoxic double perovskite scintillators, *Light: Sci. Appl.*, 2020, **9**, 112.
10 Z. Wang, X. Xu, S. Wang, H. Xu, W. Xu, Q. Zeng, G. Deng, Y. Jiang and S. Wu, Cerium doping double perovskite scintillator for sensitive X-ray detection and imaging, *Chem. – Eur. J.*, 2021, **27**, 9071–9076.
11 D. Chen, G. Niu, S. Hao, L. Fan, J. Zhao, C. Wolverton, M. Xia and Q. Liu, Decreasing structural dimensionality of double perovskites for phase stabilization toward efficient X-ray detection, *ACS Appl. Mater. Interfaces*, 2021, **13**, 61447–61453.
12 D. Kowal, M. Makowski, M. E. Witkowski, R. Cala, M. A. Kuddus Sheikh, M. H. Mahyuddin, E. Auffray, W. Drozdowski, D. Cortecchia and M. D. Birowosuto, PEA_2PbI_4: fast two-dimensional lead iodide perovskite scintillator with green and red emission, *Mater. Today Chem.*, 2023, **29**, 101455.
13 X. Zhang, S. Yu, X. Meng and S. Xiao, A review on lead-free perovskites for X-ray detection and imaging, *Cryst. Res. Technol.*, 2023, **58**, 2200232.
14 H. Peng, W. Huang, L. Kong, S. Yu and B. Zou, All-in-one double perovskite flexible film with highly efficient warm-white emission, near-infrared emission, and X-ray radioluminescence, *Adv. Funct. Mater.*, 2025, **35**, 2422745.
15 H. Siddique, Evidence and engineering of x-ray luminescence in lead free perovskite $Cs_2AgInCl_6$ with Bi substitutions, *APL Mater.*, 2024, **12**, 101101.
16 H. Rong, X. Xu, J. Y. Yao, Q. Fan, H. Zhang, H. Xu, J. Luo, Q. Chen and Z. Sun, High-resolution flexible X-ray imaging in a two-dimensional Mn^{2+}-doped perovskite scintillator, *ACS Appl. Mater. Interfaces*, 2025, **17**, 24137–24145.
17 H. Xu, W. Liang, Z. Zhang, C. Cao, W. Yang, H. Zeng, Z. Lin, D. Zhao and G. Zou, 2D Perovskite Mn^{2+} -Doped

$Cs_2CdBr_2Cl_2$ scintillator for low-dose high-resolution X-ray imaging, *Adv. Mater.*, 2023, **35**, e2300136.

18 T. Chen, D. Mu, F. Lin, W. Tang, Y. Zhou, X. Shi, C. Li, X. Jiang, X. Li, H. Chen, T. Chen, X. Xu and C. Wang, 1D Cs_2AgBr_3:Mn^{2+} crystals to realize high-resolution X-ray scintillation imaging, *J. Mater. Chem. C*, 2025, **13**, 5771–5778.

19 Q. Fan, H. Zhang, S. You, Y. Liu, P. Zhu, H. Xu, W. Guo, Y. Ma, J. Luo, Y. Liu and Z. Sun, Dion–jacobson phase Mn^{2+}–doped perovskite scintillators for high–resolution X–ray imaging, *Laser Photonics Rev.*, 2024, **19**, 2401674.

20 L. Han, X. Yuan, Z. Wang, J. Hua, J. Wang, J. Zheng and J. Zhao, Boosted luminescence efficiency and stability of Mn-doped perovskite nanoplatelets via incorporating Cd^{2+} ions, *Mater. Res. Bull.*, 2022, **151**, 111825.

21 N. Nandha K and A. Nag, Synthesis and luminescence of Mn-doped $Cs_2AgInCl_6$ double perovskites, *Chem. Commun.*, 2018, **54**, 5205–5208.

22 F. Locardi, M. Cirignano, D. Baranov, Z. Dang, M. Prato, F. Drago, M. Ferretti, V. Pinchetti, M. Fanciulli, S. Brovelli, L. De Trizio and L. Manna, Colloidal synthesis of double perovskite $Cs_2AgInCl_6$ and Mn-doped $Cs_2AgInCl_6$ nanocrystals, *J. Am. Chem. Soc.*, 2018, **140**, 12989–12995.

23 L. Zhang, X. Xie, D. Li, Y. Yuan, X. Xue, Q. Li, J. Xu, H. Wang, F. Hu and X. Zhang, Investigation on lead-free Mn-doped $Cs_2NaInCl_6$ double perovskite phosphors and their optical properties, *Opt. Mater.*, 2021, **122**, 111802.

24 S. Banerjee, S. Saikia, M. S. Molokeev and A. Nag, Unveiling Temperature-Induced Structural phase transition and luminescence in Mn^{2+}-Doped $Cs_2NaBiCl_6$ double perovskite, *Chem. Mater.*, 2024, **36**, 4750–4757.

25 D. Chen, C. Wu, H. Li, L. Zhou, P. Chen, Q. Pang, X. Zhang and J. Z. Zhang, Near-infrared emission, energy transfer, and mechanisms of Mn^{2+} and Cr^{3+} Co-doped lead-free $Cs_2AgInCl_6$ double perovskites, *J. Mater. Chem. C*, 2023, **11**, 12649–12657.

26 S. Xu, G. Zhang, R. Wang, X. Li, H. Zhang and C. Su, Red-blue dual emission and enhanced luminescence of glass-ceramics containing $Y_2Sn_2O_7$ for plant lighting, *J. Alloys Compd.*, 2025, **1010**, 178098.

27 Y. Zhong, N. Zhou, M. Xia, Y. Zhou, H. Chen and Z. Zhou, Synthesis and photoluminescence properties of novel red-emitting phosphor $SrAl_3BO_7$:Mn^{4+} with enhanced emission by Mg^{2+}/Zn^{2+}/Ca^{2+} incorporation for plant growth LED lighting, *Ceram. Int.*, 2019, **45**, 23528–23539.

28 L. Zheng, L. Zhang, L. Fang, H. Wu, H. Wu, G. H. Pan, Y. Yang, Y. Luo, Z. Hao and J. Zhang, Be^{2+}–induced red emission enhancement in $CaAl_{12}O_{19}$:Mn^{4+} for wide color gamut display: suppressing self–reduction of Mn^{4+} to Mn^{2+}, *Adv. Opt. Mater.*, 2023, **12**, 2301480.

29 E. Cui, X. Yuan, L. Tang, L. Yang, X. Yang, X. Liao, J. Tang, Y. Zhao, W. Sun, K. Liu, Y. Liu and J. Liu, Eu^{3+}, Tb^{3+} doping induced tunable luminescence of $Cs_2AgInCl_6$ double perovskite nanocrystals and its mechanism, *Appl. Surf. Sci.*, 2023, **609**, 155472.

30 Y. Liu, X. Rong, M. Li, M. S. Molokeev, J. Zhao and Z. Xia, Incorporating rare-earth terbium(III) ions into $Cs_2AgInCl_6$: Bi nanocrystals toward tunable photoluminescence, *Angew. Chem., Int. Ed.*, 2020, **59**, 11634–11640.

31 R. Xu, B. Zheng, X. Fang, X. Sun, J. Hong, H. Huang, W. Wang and J. Wang, Visible to near-infrared luminescence and reversible photochromism in Mn^{2+}/Nd^{3+} co-doped double perovskite for versatile applications, *Adv. Opt. Mater.*, 2025, **13**, 2402515.

32 W. Fan, L. Meng, S. Sun, H. Wei, Q. Kong, Y. Wu and B. Cao, Achieving multi-excitation in lanthanide-based $Cs_2NaTbCl_6$:Ce/Yb double perovskite single crystals for anti-counterfeiting, *Ceram. Int.*, 2024, **50**, 41802–41809.

33 H. Arfin, R. Rathod, A. S. Shingote, K. R. Priolkar, P. K. Santra and A. Nag, Short-wave infrared emissions from Te^{4+}–Ln^{3+} (Ln: Er, Yb)-codoped $Cs_2NaInCl_6$ double perovskites, *Chem. Mater.*, 2023, **35**, 7133–7143.

34 J. Qiang, H. Ruan, L. Wang, T. Wang, J. Lei, S. Liao and S. Li, Luminescence enhancement of K_2LiAlF_6:Mn^{4+} phosphors by Zn^{2+}-mediated charge compensation for fast-response backlighting applications, *Inorg. Chem.*, 2023, **62**, 14344–14354.

35 W. Fan, L. Meng, S. Sun, H. Wei, Q. Kong, Y. Wu and B. Cao, Achieving multi-excitation in lanthanide-based $Cs_2NaTbCl_6$:Ce/Yb double perovskite single crystals for anti-counterfeiting, *Ceram. Int.*, 2024, **50**, 41802–41809.

36 S. K. Gupta and K. Sudarshan, Effect of Zr^{4+} and Hf^{4+} substitution at Sn-site on luminescence properties of Eu^{3+} doped $CaSnO_3$ perovskite, *Inorg. Chem. Commun.*, 2024, **164**, 112400.

37 L. Jiang, L.-K. Wu, Q.-H. Zou, J.-L. Bai, H.-Y. Ye and J.-R. Li, Thermoplastic zero-dimensional hybrid indium halide achieving orange emission and scintillation properties triggered by Sb^{3+}/Mn^{2+} doping, *Inorg. Chem.*, 2025, **64**, 11252–11259.

38 H. Xu, W. Liang, Z. Zhang, C. Cao, W. Yang, H. Zeng, Z. Lin, D. Zhao and G. Zou, 2D perovskite Mn^{2+}-doped $Cs_2CdBr_2Cl_2$ scintillator for low-dose high-resolution X-ray imaging, *Adv. Mater.*, 2023, **35**, 2300136.

39 Q. Fan, H. Zhang, S. You, Y. Liu, P. Zhu, H. Xu, W. Guo, Y. Ma, J. Luo, Y. Liu and Z. Sun, Dion-Jacobson phase Mn^{2+}-doped perovskite scintillators for high-resolution X-Ray imaging, *Laser Photonics Rev.*, 2025, **19**, 2401674.

40 L. Fei, L. Yang, P. Li and J. Ma, Unlocking Near 100% PLQY: The Impact of post–treatment on emission efficiency of Mn^{2+}:$CsPbCl_3$ nanocrystals, *Adv. Opt. Mater.*, 2024, **13**, 2402826.

41 J. Tong, J. Huan, X. Yu, J.-H. Cheng, Z.-J. Zhang, J.-J. Xing, J.-T. Zhao and X.-X. Yang, Significantly enhanced mechanoluminescence from Nb^{5+} co-doped ZrO_2:Sm^{3+} via a high valence ion doping strategy, *J. Mater. Chem. C*, 2023, **11**, 11597–11605.

42 L. Zheng, Y. Yang, H. Wu, H. Wu, G. H. Pan, Y. Luo, Z. Hao, L. Zhang and J. Zhang, Toward controllable self–reduction of Mn^{4+} to Mn^{2+} by lanthanide ions for luminescence based colorimetric sensing of temperature, *Adv. Opt. Mater.*, 2024, **13**, 2402020.

43 B. Priyadarshini, U. Anjaneyulu and U. Vijayalakshmi, Preparation and characterization of sol-gel derived Ce^{4+} doped hydroxyapatite and its in vitro biological evaluations for orthopedic applications, *Mater. Des.*, 2017, **119**, 446–455.

44 H. Y. Hong, D. H. Kim, S. O. Won and K. Park, Enhancement of the thermoelectric performance of n–type Bi_2O_2Se by Ce^{4+} doping, *J. Mater. Res. Technol.*, 2021, **15**, 4161–4172.

45 Y. Yan, C. Luo, S. Ling, J. Liang, S. Liao and Y. Huang, Deep-red emission in Mn^{4+} activated $CaMgAl_{10}O_{17}$ phosphor and enhanced optical photoluminescence by charge compensator of Mg^{2+}, *Opt. Mater.*, 2022, **132**, 112818.

46 M. M. Afandi and J. Kim, Strategies for fourfold enhancement of narrowband green AC-driven electroluminescence from zinc gallate co-doped with Ce^{3+} and Mn^{2+} ions by field-enhanced energy transfer, *J. Alloys Compd.*, 2023, **967**, 171622.

47 M. Puchalska and A. Watras, A clear effect of charge compensation through Na^{+} co-doping on luminescent properties of new $CaGa_4O_7:Nd^{3+}$, *J. Alloys Compd.*, 2016, **688**, 253–260.

48 J. Li, Z. Tu, Y. Zheng, Q. Zeng, Q. Hu, Q. Li, X. Xiang, Y. Kong, H. Zhang, B. Wang and J. Zhu, Zero-thermal-quenching and charge compensation for efficient luminescence in $Ca_9ZnK(PO_4)_7:Sm^{3+}$: Optimizing defect engineering, *Ceram. Int.*, 2024, **50**, 9869–9877.

49 F. Ruan, G. Fan, N. Li, J. Zhou, Y. Li, D. Fan, Q. Chen and Z. Lin, Charge compensation effect of alkali metal ions on luminescence enhancement and negative thermal quenching of $Sr_{1(-x}LaNaTeO_6:_xEu^{3+}$ red phosphors, *Ceram. Int.*, 2024, **50**, 12866–12876.

50 B. Su, K. Han and Z. Xia, Mn^{2+}-doped Cs_2ZnBr_4 scintillator for X-ray imaging, *J. Mater. Chem. C*, 2023, **11**, 8052–8061.

51 F. Zhang, Y. Zhou, Z. Chen, X. Niu, H. Wang, M. Jia, J. Xiao, X. Chen, D. Wu, X. Li, Z. Shi and C. Shan, Large–area X–ray scintillator screen based on cesium hafnium chloride microcrystals films with high sensitivity and stability, *Laser Photonics Rev.*, 2023, **17**, 2204801.

52 K. Han, J. Jin, Y. Wang, X. Zhou, Y. Sun, L. Chen and Z. Xia, Hybrid Eu(II)-bromide scintillators with efficient 5d4f bandgap transition for X-ray imaging, *Light: Sci. Appl.*, 2024, **13**, 222.

53 Z. Zeng, G. Zhang, Y. Wang, M. Zhang, Z. Cheng, H. Lian and J. Lin, Mn^{2+}/Er^{3+}-codoped $Cs_2AgInCl_6$ double perovskites with dual emission and photochromism properties for anti-counterfeiting application, *Laser Photonics Rev.*, 2024, **18**, 2300983.